Learning-based inversion method for solving electromagnetic inverse scattering with mixed boundary conditions

Rencheng Song *Member, IEEE*, Youyou Huang, Xiuzhu Ye *Senior Member, IEEE*, Kuiwen Xu *Member, IEEE*, Chang Li *Member, IEEE* and Xun Chen *Senior Member, IEEE*

***Abstract*—In this paper, a unified learning-based approach is introduced to solve inverse scattering problems (ISPs) with mixed boundary conditions. The scattering behavior of hybrid dielectric and perfect electric conductors (PEC) scatterers is modeled by the T-matrix method. A rough image of the zero-order T-matrix coefficients for unknown scatterers is firstly reconstructed by the back-propagation method, which is then refined by an attention-assisted pix2pix generative adversarial network. The spatial attention mechanism is utilized to enforce the generator network to learn salient features of the unknown scatterers instead of the background. The adversarial training of the generator and the discriminator further enables the reconstructed image to be constrained by high-level features of reference scatterers. Numerical tests on both synthetic and experimental data verify the superior performance of the proposed method for ISP reconstructions with hybrid scatterers. It effectively expands the application scope of learning-based ISP methods to reconstruct scatterers without knowing the boundary conditions of scatterers in advance.**

***Index Terms*—Inverse scattering, generative adversarial network, T-matrix, mixed boundary conditions.**

I. Introduction

THE objective of inverse scattering problems (ISPs) is to determine the position, shape, and parameters of unknown scatterers based on the measurement of scattered field [1]. The fast and high-quality reconstruction of ISPs is urgently demanded in many areas [2]–[4]. After decades of development, various inverse scattering algorithms have been proposed. As far as we know, most existing methods are designed with prior information on the physical properties of unknown scatterers. For example, the scatterers are assumed a priori to be dielectric [5]–[7] or perfect electric conductor (PEC) [8]–[10]. However, it is common that the information of boundary conditions (BCs) for unknown scatterers is lacking in ISPs. Particularly, the PEC and dielectric scatterers may both be presented in the domain of interest (DOI).

To solve ISPs with mixed BCs, the forward scattering of hybrid scatterers needs to be modeled under a uniform framework. The T-matrix method introduced by Waterman [11] has the ability to deal with scattering with mixed BCs. Inspired by the pioneering work [12]–[14], Ye et al. [15] firstly proposed to simultaneously reconstruct dielectric and PEC scatterers using the T-matrix method. They reformulated the subspace based optimization method (SOM) [7] with the T-matrix modeling to deal with the mixed BC problem. The authors also introduced a classification criteria to classify the PEC scatterers from the dielectric ones based on the obtained T-matrix coefficients. Later, Song et al. [16] further extended this method to reconstruct scatterers with at most four types of BCs. The methods [15], [16] have been verified to be very efficient for reconstructing scatterers without prior information on their physical properties. However, the nonlinear iterative T-matrix methods [15], [16] are usually time-consuming, since the multi-pole expansions greatly increase the computational burden.

In recent years, considering the advantages on speed and reconstruction quality, deep learning techniques have been widely used to solve electromagnetic ISPs [17], [18]. The learning-based inversion methods can be generally divided into three types [18]. The first type of methods directly reconstruct the permittivity of scatterers from the measured scattered field [19]–[21]. This kind of methods need to fully learn the governing physics of the inversion, which is a very challenging task. The second type of methods still follow the iterative framework to solve the ISPs as a optimization of cost functions,

This work was supported in part by the National Natural Science Foundation of China (Grants 61922075, 61971174, 41901350), in part by the Provincial Natural Science Foundation of Anhui (Grants 2108085MF201, 2008085QF285), in part by the Aeronautical Science Foundation of China (Grant 20181837002), and in part by the Fundamental Research Funds for the Central Universities (Grants PA2021KCPY0051, JZ2021HGTB0078). (Corresponding author: Xiuzhu Ye and Xun Chen).

R. Song, Y. Huang and C. Li are with the Department of Biomedical Engineering, and also with the Anhui Province Key Laboratory of Measuring Theory and Precision Instrument, Hefei University of Technology, Hefei 230009, China (e-mail:rcsong@hfut.edu.cn; huangyy@mail.hfut.edu.cn; changli@hfut.edu.cn).

X. Ye is with School of Information and Electronics Engineering, Beijing Institute of Technology, Beijing, China (email:xiuzhuye@outlook.com)

K. Xu is with Engineering Research Center of Smart Microsensors and Microsystems, Ministry of Education, Hangzhou Dianzi University, Hangzhou 310018, China (e-mail: kuiwenxu@hdu.edu.cn).

Xun Chen is with Department of Neurosurgery, the First Affiliated Hospital of USTC, Division of Life Sciences and Medicine, and also with the Department of Electronic Engineering and Information Science, University of Science and Technology of China, Hefei, Anhui, 230001, China (e-mail: xunchen@ustc.edu.cn).

which enforce physical match of measurements [22]–[24]. The deep learning techniques are incorporated into the iterative frameworks to overcome the bottleneck of conventional iterative methods. The third type of methods design the reconstruction algorithms by incorporating domain knowledge into the networks, which are called physics-inspired learning approach [20], [25]–[28]. A typical way of physics-inspired learning approach is that it decouples the full-wave model into a two-step reconstruction. The scattered field is firstly taken to get a rough reconstruction by fast imaging methods like backpropagation (BP) [1]. Neural networks are then employed to further enhance the quality of the rough input image through building a mapping with its reference one. In contrast, Guo et al. [28] introduces an iterative deep neural network to enforce the match of scattered filed in the 2D case. The existing learning-based inversion methods have achieved great success in terms of computational speed and imaging quality. However, these existing learning-based methods are only designed to solve ISPs with known BCs, and most of the methods only consider the reconstruction of dielectric scatterers.

In this paper, we introduce a unified learning-based method to reconstruct scatterers for ISPs with mixed BCs. The proposed method follows the framework of physics-inspired learning approach. It decouples the full-wave inversion into a two-step reconstruction. Particularly, the scattering of hybrid scatterers is modeled by the T-matrix method. A rough reconstruction of zero-order T-matrix coefficients is firstly obtained by the BP method, which is then refined by an attention-assisted pix2pix generative adversarial network (GAN) [29]. The spatial attention mechanism is incorporated into the U-net-like [30] generator network to highlight the feature learning on the unknown scatterers. The adversarial training of the generator and the discriminator enables the reconstruction to be constrained by high-level features of reference scatterers. Finally, a balancing treatment is introduced to deal with the distinct magnitude scales of T-matrix coefficients for PEC and dielectric scatterers, thereby improving the training of model. The proposed method is tested with both synthetic and experimental data and it achieves satisfactory imaging results for ISP with mixed BCs.

In summary, the benefits of the proposed method are listed as below:

1) First, we introduce a unified model to reconstruct scatterers with different BCs. The zero-order T-matrix coefficients instead of the commonly used relative permittivity are reconstructed through the learning-based model without knowing the type of scatterers in advance. To the best of our knowledge, it is the first time that the learning-based approach is introduced to solve the ISP with mixed BCs.
2) Second, a spatial attention is incorporated into the pix2pix GAN to highlight the feature learning on the unknown scatterers. The use of spatial attention mechanism, together with the guidance by the discriminator, effectively improves the quality of reconstruction. Meanwhile, the use of only zero-order T-matrix coefficients greatly accelerates the reconstruction speed compared to nonlinear iterative ISP methods.
3) Third, we propose a way to balance the T-matrix coefficients of PEC and dielectric scatterers in the reference images of the training data set. It effectively improves the convergence of network training, and it is also beneficial to enhance the performance to reconstruct hybrid scatterers.

The structure of this paper is as follows. In Section II, we introduce the formulations of the proposed method. Numerical verifications of this method are condutcted in Section III by both synthetic and experimental data. Finally, we conclude our work in Section IV.

II. DESCRIPTION OF THE ALGORITHM

A. Formulation of the problem

In this paper, we consider a two-dimensional (2-D) transverse magnetic (TM) scattering problem as depicted in Fig. 1. Suppose there are at most two types of nonmagnetic scatterers, the dielectric and the PEC scatterers, located inside the domain of interest (DOI) D. There are N_i plane waves illuminated evenly from transmitters (Tx) outside D. For each incidence, the scattered fields are measured by N_r receivers (Rx) located at a circle S outside D.

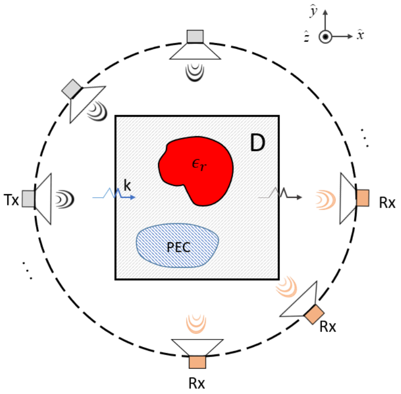

Fig. 1. Sketch of scattering problem with mixed BCs.

Let the DOI D be discretized into subunits. According to the definition of T-matrix, the relation of scattered filed and the incident field on the ith subunit within D can be expressed as follows

$$\bar{a}_i = \bar{\bar{T}}_i \cdot [\bar{e}_i + \sum_{j=1,j\neq i}^{N} \bar{\bar{\alpha}}_{ij} \cdot \bar{a}_j], \tag{1}$$

where $\bar{a}_i$ refers to the amplitude vector of the induced multipoles, $\bar{e}_i$ indicates the vector of multipole expansion coefficients for the incident field, $\bar{\bar{\alpha}}_{ij}$ is the translational matrix, and $\bar{\bar{T}}_i$ is the diagonal T-matrix coefficient matrix of the ith subunit.

Particularly, the mth-order T-matrix coefficient of a dielectric scatterer is [31]

$$[\bar{\bar{T}}]_m = \frac{kJ_m(k_0R)J_m'(kR) - k_0J_m(kR)J_m'(k_0R)}{k_0H_m^{(1)'}(k_0R)J_m(kR) - kJ_m'(kR)H_m^{(1)}(k_0R)}, \tag{2}$$

where J_m is the mth-order Bessel function of the first kind, $H_m^{(1)}$ indicates the mth-order Hankel function of the first kind, k_0 is the wavenumber of the incident wave in background medium, $k = k_0\sqrt{\epsilon_r}$ is the wavenumber of the incident wave in the scatterer with ϵ_r as the relative permittivity, and R is the equivalent radius of each subunit.

Similarly, the mth-order T-matrix coefficient of PEC is

$$[\bar{\bar{T}}]_m = -\frac{J_m(k_0R)}{H_m^{(1)}(k_0R)}. \tag{3}$$

The explicit expressions of all the other variables in Eq. (1) can be found in [15] or the literatures inside.

For a single incidence, we combine the Eq. (1) on each subunits into one matrix equation as

$$\bar{a} = \bar{\bar{O}} \cdot [\bar{e} - \bar{\bar{A}} \cdot \bar{a}], \tag{4}$$

where $\bar{\bar{O}}$ is a block diagonal matrix with $[\bar{\bar{O}}]_{ii} = \bar{\bar{T}}_i$, $[\bar{\bar{A}}]_{ij} = -\bar{\bar{\alpha}}_{ij}$ for $i \neq j$ and zero otherwise, $[\bar{a}]_i = \bar{a}_i$ and $[\bar{e}]_i = \bar{e}_i$.

After getting the amplitude vector $\bar{a}$, the scattered field vector $\bar{E}^{sca}$ at all N_r receivers can be obtained by

$$\bar{E}^{sca} = \bar{\bar{\Psi}}^t \cdot \bar{a}, \tag{5}$$

where t indicates the transpose, $\bar{\bar{\Psi}}$ represents the mapping which maps $\bar{a}$ within D to $\bar{E}^{sca}$ on receivers.

Eqs. (4) and (5) are referred to as the state equation and the field equation, respectively. In the forward scattering problem, with given T-matrix coefficients $\bar{\bar{O}}$ and incidence expansion $\bar{e}$, the purpose is to calculate the unknown $\bar{E}^{sca}$ and $\bar{a}$ by these two equations. The advantage of the T-matrix modeling is that it can uniformly model the scattering of scatterers with different BCs.

In contrast, the inversion aims to reconstruct the T-matrix coefficients $\bar{\bar{O}}$ through measured scattered fields $\bar{E}^{sca}$ and the corresponding incidence expansion $\bar{e}$. According to Eqs. (4) and (5), the cost function of ISP with the jth incidence can be directly built as

$$\begin{aligned} f_j(\{\bar{a}\}_j, \bar{\bar{O}}) = &\frac{1}{2}\Big(\|\{\bar{E}^{sca}\}_j - \bar{\bar{\Psi}}^t \cdot \{\bar{a}\}_j\|^2/\|_2\{\bar{E}^{sca}\}_j\|_2^2 \\ &+ \|\{\bar{a}\}_j - \bar{\bar{O}} \cdot [\{\bar{e}\}_j - \bar{\bar{A}} \cdot \{\bar{a}\}_j]\|_2^2/\|\{\bar{e}\}_j\|_2^2\Big), \end{aligned} \tag{6}$$

where $\|\cdot\|_2$ represents the l^2 norm, $\{\cdot\}_j$ indicates the full resulting vector of $\{\cdot\}$ for the jth incidence. The unknowns are the T-matrix coefficients $\bar{\bar{O}}$ and the multipole expansion coefficient $\bar{a}$ with respect to the current incidence.

For all N_i incidences, the total cost functional F can be given as

$$F(\{\bar{a}\}_{j=1,2,\ldots,N_i}, \bar{\bar{O}}) = \sum_{j=1}^{N_i} f_j(\{\bar{a}\}_j, \bar{\bar{O}}), \tag{7}$$

where $\{\bar{a}\}_{j=1,2,\ldots,N_i}$ indicate the $\bar{a}$ for all N_i incidences, and f_j is the cost function in Eq. (6) for the jth incidence.

In [15], the cost functional F in Eq. (7) is reformulated under the framework of SOM by decomposing $\bar{a}$ into the deterministic part and the ambiguous part, where the former one can be easily determined by the singular value decomposition of $\bar{\bar{\Psi}}^t$. The $\{\bar{a}\}_{j=1,2,\ldots,N_i}$ and the T-matrix coefficients $\bar{\bar{O}}$ can be updated alternatively by a gradient-based optimization in SOM. It is found that the T-matrix SOM [15] can efficiently solve the ISP with mixed BCs and it performs robustly in presence of noise.

After the retrieval of T-matrix coefficients $\bar{\bar{O}}$, the physical property of scatterers can be distinguished by the asymptotic expansions for the zeroth-order T-matrix coefficient $[T]_0$ with small k_0R [15], [16]. The imaginary part of $[T]_0$ for PEC scatterer is negative, while that of the dielectric scatterer is positive. This paper will also use this criterion to distinguish the two types of scatterers from the reconstruction results.

B. The unified learning-based ISP method

The flowchart of the proposed method for solving ISP with mixed BCs is illustrated in Fig. 2. As shown, the coarse image x of $[T]_0$ is reconstructed by the BP method, which serves as the input of the attention-assisted pix2pix GAN model. The generator G_θ in the pix2pix model aims to reconstruct high-quality $G_\theta(x)$, which approximates the reference $[T]_0$ image y. The discriminator network D_ϕ is taken to guide the G_θ through the adversarial training.

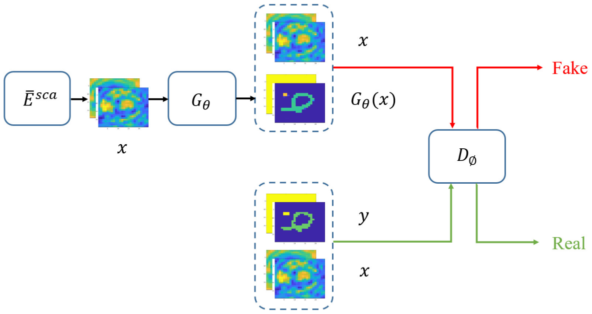

Fig. 2. The flowchart of the learning-based T-matrix method. The input image x is consisted of raw zero-order T-matrix coefficient $[T]_0$ constructed by BP, while the generated $G_\theta(x)$ aims to approximate the reference $[T]_0$ denoted as y. The mapping is learned under the framework of conditional generative adversarial networks, where the input x is taken as the condition in the input of discriminator D_ϕ.

1) Fast reconstruction of coarse $[T]_0$ image x: To guarantee the speed of the whole method, in this paper, the BP method [1], [32] is taken to reconstruct the rough image x of $[T]_0$. The details are described as below.

First, we assume that the full amplitude vector of induced multipole $\bar{a}$ satisfies $\bar{a} = \gamma \cdot (\bar{\bar{\Psi}}^t)^{\mathrm{H}} \cdot \bar{E}^{sca}$, where the superscript H denotes the conjugate transpose operation, and γ is the unknown complex scaling coefficient.

The complex γ can be explicitly obtained through minimizing the following objective function

$$F(\gamma) = \|\bar{E}^{sca} - \bar{\bar{\Psi}}^t \cdot \gamma \cdot (\bar{\bar{\Psi}}^t)^{\mathrm{H}} \cdot \bar{E}^{sca}\|_2^2, \tag{8}$$

where we can get

$$\gamma = \frac{\left\langle \bar{E}^{sca}, \bar{\bar{\Psi}}^t \cdot \left((\bar{\bar{\Psi}}^t)^{\mathrm{H}} \cdot \bar{E}^{sca} \right) \right\rangle_S}{\left\| \bar{\bar{\Psi}}^t \cdot \left((\bar{\bar{\Psi}}^t)^{\mathrm{H}} \cdot \bar{E}^{sca} \right) \right\|_S}. \tag{9}$$

Here $\langle \cdot, \cdot \rangle_S$ denotes the inner product of two vectors on the measurement circle S.

After getting $\bar{a}$, we further obtain vector $\bar{b}$ as $\bar{b} = \bar{e} - \bar{\bar{A}} \cdot \bar{a}$. The above process is repeated for all N_i incident waves.

Finally, taking into account of the relation $\bar{a} = \bar{\bar{O}} \cdot \bar{b}$, we can get the diagonal vector $\bar{O}$ of $\bar{\bar{O}}$ as the solution of a least-squares problem

$$\bar{O} = \left(\sum_{p=1}^{N_i} \{\bar{a}\}_p \odot \{\bar{b}\}_p^* \right) \oslash \left(\sum_{p=1}^{N_i} \{\bar{b}\}_p \odot \{\bar{b}\}_p^* \right), \tag{10}$$

where $\{\cdot\}_p$ indicates the vector $\bar{a}$ or $\bar{b}$ corresponding to the pth incidence, $\odot$ indicates the element-wise product, $\oslash$ represents the element-wise division, and $(\cdot)^*$ is the conjugate operation of the complex vector $(\cdot)$. The rough input image x of $[T]_0$ can then be obtained by reshaping $\bar{O}$ in Eq.(10).

2) The spatial-attention-assisted pix2pix network: In this paper, the generator G_θ is taken as the attention U-net [30] as shown in Fig. 3. The rough image x of $[T]_0$ is decomposed as the real and imaginary parts that serve as the input of the generator.

It can be seen in Fig. 3 that the attention U-net architecture consists of three branches. The encoding branch on the left is to extract different levels of feature maps, while the decoding branch on the right is to reconstruct the image through deconvolutions of corresponding features. Besides, the spatial attention gate (AG) module is used to guard the output features of the encoder, which generates a gating signal g to control the importance of features at different spatial locations. The use of the spatial AG module can highlight the feature learning on scatterers for the generator network, which helps to improve the quality of the reconstruction.

The AG module for the lth layer in Fig. 3 generates a weight map α_i^l as

$$q_{att}^l = \psi^t(\sigma_1(W_x^t x_i^l + W_g^t g_i + b_g)) + b_\psi \tag{11}$$

$$\alpha_i^l = \sigma_2(q_{att}^l(x_i^l, g_i; \Theta_{att})) \tag{12}$$

where W_x, W_g and ψ are linear transformation vectors, b_ψ and b_g are bias terms, t denotes the transpose, Θ_{att} represents the set of all unknown parameters of AG including $\{W_x, W_g, \psi, b_\psi, b_g\}$, $\sigma_1(z) = \max(0, z)$ is the rectified linear unit activation function, and $\sigma_2(z) = \frac{1}{1+\exp(-z)}$ is the sigmoid activation function. x_i^l represents the feature vector corresponding to the ith spatial position of the lth layer of the encoder, while g_i represents the gate signal at the same spatial position. The output of AG $\hat{x}_i^l$ is the element-wise multiplication of the input feature-maps x_i^l and attention coefficients α_i^l:

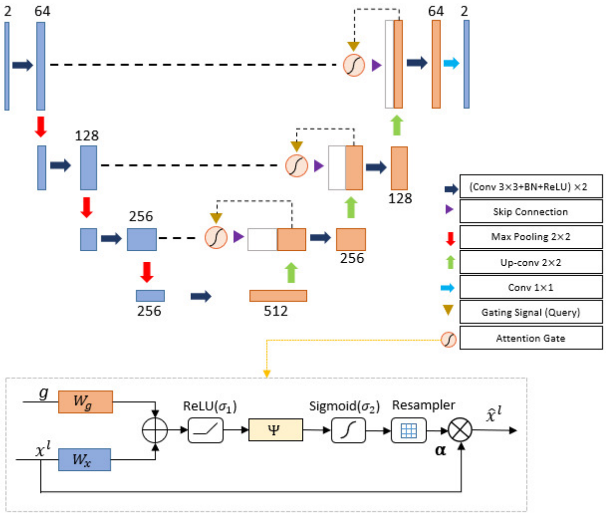

Fig. 3. The structure of the attention-assisted generator.

$$\hat{x}_i^l = x_i^l \odot \alpha_i^l. \tag{13}$$

The discriminator network D_ϕ is illustrated in Fig. 4. The goal of D_ϕ is to distinguish the reconstructed image $G_\theta(x)$ from the real image y. The input of D_ϕ is the reconstructed image $G_\theta(x)$ or the real target image y, conditioned by the rough input image x. The output of D_ϕ is a feature discrimination matrix defined on the patches of inputs [29].

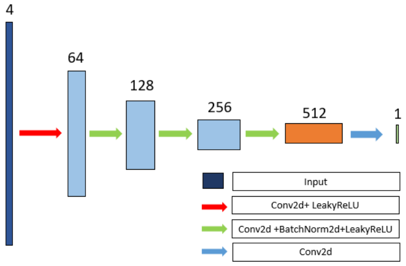

Fig. 4. The structure of the discriminator.

3) The loss functions: The loss function of generator G_θ is defined as (14)

$$L_G(\theta) = \alpha L_1(\theta) + L_A(\theta|\phi), \tag{14}$$

where $L_1(\theta)$ denotes the pixel-wise loss between the reconstructed image and the reference one, $L_A(\theta|\phi)$ indicates the adversarial loss with fixed ϕ, and α is a weighing parameter to balance the two losses. Particularly, the

$L_1(\theta)$ and $L_A(\theta|\phi)$ losses are defined as

$$L_1(\theta) = \frac{1}{N}\left(\sum_{i=1}^{N} \|G_\theta(x_i) - y_i\|_1\right) \tag{15}$$

$$L_A(\theta|\phi) = \frac{1}{N}\sum_{i=1}^{N}\left(D_\phi(G_\theta(x_i)) - 1\right)^2, \tag{16}$$

respectively, where N indicates the batch size and $\|\cdot\|_1$ represents the l^1 norm.

The loss function of discriminator D_ϕ is

$$L_D(\phi|\theta) = \frac{1}{2N}\sum_{i=1}^{N}\left((D_\phi(y_i) - 1)^2 + (D_\phi(G_\theta(x_i)))^2\right), \tag{17}$$

where ϕ is the unknown parameter tensor and θ is fixed.

Since G_θ and D_ϕ are optimized alternatively, the parameter tensor of one network is fixed when we update the other one. The two neural networks will be trained in an adversarial way until reaching a Nash-equilibrium.

4) Balancing treatment of $[T]_0$ for hybrid scatterers: According to definitions in Eqs. (2) and (3), the $[T]_0$ of dielectric and PEC scatterers have quite distinct magnitudes, where the $[T]_0$ of the dielectric scatterer is much smaller than that of the PEC one. To avoid that the training model is biased towards PEC type scatterers, we propose to scale the $[T]_0$ of PEC scatterers to a similar magnitude as the dielectric one.

It is noted that the scaling is only implemented on the reference image y in the training data set that contains PEC scatterers. First, the PEC and dielectric scatterers in the reference images of the training set are both represented as the true T-matrix coefficient $[T]_0$. The $[T]_0$ of true PEC scatterers is then scaled to a similar magnitude as the dielectric one. In contrast, the rough BP input image of $[T]_0$ retains its original scale, since it is difficult to distinguish the PEC scatterer from the dielectric one by the raw input BP image in the testing phase. However, we can easily identify the PEC scatterers after we get the inversion results of $G_\theta(x)$. The true magnitude of $[T]_0$ for PEC scatterers can then be recovered with the known scaling coefficient. The above balancing treatment eases the difficulty of training the network and more details about the scaling are given as below.

Since the magnitudes of $[T]_0$ for dielectric and PEC scatterers are both dominated by their imaginary parts, we first calculate the ratio of $\text{imag}([T]_{0,PEC})/\text{imag}([T]_{0,diel})$, where $\text{imag}([T]_{0,diel})$ indicates the imaginary part of dielectric $[T]_0$ calculated by the relative permittivity ε_r appearing the highest frequency in the training data set. Finally, we search for the best scaling coefficient C near this ratio.

After C is obtained, the $[T]_0$ of PEC scatterers will be divided by C if there are PEC scatterers in each reference image y. The balancing treatment is done for all samples with PEC scatterers, even for the sample with only PEC scatterers. The reason is that there exists four different combinations of scatterers in the training data set. The reference images $\{y\}$ of all training samples are expected to maintain similar magnitudes after processing.

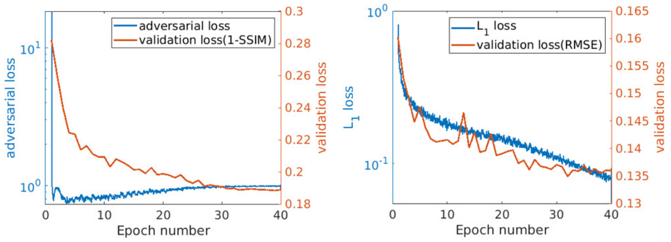

Fig. 5. The training and validation loss curves of the proposed Att-GAN method. The left one is the adversarial loss and the validation loss defined by 1-SSIM, while the right one is the L_1 loss and the validation loss defined by RMSE.

In testing, the original input image x is still taken to get the reconstructed $G_\theta(x)$, which approximates the normalized reference image y. We first identify whether there exists PEC scatterers in $G_\theta(x)$ according to the property of $[T]_0$ as described in Section II-A. If so, the $[T]_0$ of PEC scatterers will be multiplied by the same C as the training set to retrieve the original $[T]_0$. The above balancing treatment on $[T]_0$ is expected to enhance the performance to reconstruct hybrid scatterers. And we will verify it through the experimental study.

III. Numerical and experimental results

In this section, we verify the effectiveness of the proposed algorithm (denoted as "Att-GAN") with both synthetic and experimental data. To prove the generalization capability, we will test the trained model for both the within-database case and the cross-database case. And the performance of the proposed method is compared with the SOM formulated by T-matrix [7], [15].

A. Implementation details

The Modified National Institute of Standards and Technology (MNIST) [33] data set is taken to train the model for all examples. Besides, a random circle is also incorporated into each digit to improve the model generalization capability [26]. Each digit is randomly rotated with an angle between −170° and 170° to account for the spatial diversity of scatterers. The digit and circle are randomly set to be dielectric or PEC. Therefore, there are four possible scatterer combinations in each sample. The training data set includes 9000 samples generated from MNIST. Another 1000 samples are taken as the validation data set. All dielectric scatterers are assumed to be lossless, and the relative permittivity of the dielectric scatterers is randomly distributed between 1.1-2.5.

The first two examples are synthetic ones, while the last example is based on experimental data provided by Institut Fresnel [34]. The configurations of synthetic examples are as follows. The operating frequency is set to 300MHz, and the background medium is free space. The DOI D is chosen as a square domain with

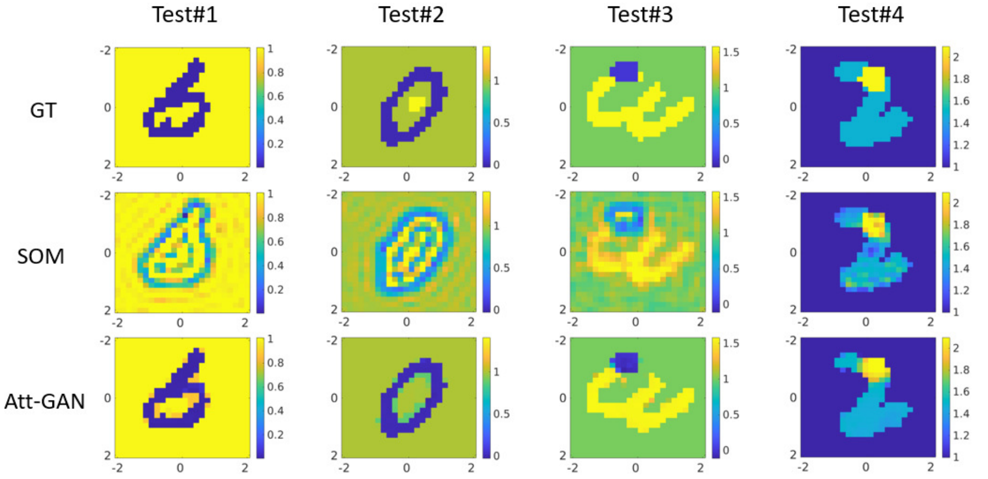

Fig. 6. Reconstruction results of Test#1 to Test#4 from the MNIST data set under 10% white Gaussian noise.

Table I
Comparison of quality metrics for reconstruction results of testing samples from MNIST data set

Test	SOM				Att-GAN			
	$E_{\varepsilon_r,diel}$	E_{pec}	E_{diel}	SSIM	$E_{\varepsilon_r,diel}$	E_{pec}	E_{diel}	SSIM
#1	/	0.5348	/	0.4167	/	0.1273	/	0.9745
#2	0.3507	0.5358	0.1344	0.4110	0.0993	0.0941	0.0628	0.9685
#3	0.1745	0.4589	0.0482	0.6511	0.1108	0.0655	0.0287	0.9459
#4	0.1264	/	0.0406	0.6912	0.1216	/	0.0304	0.9628
2500 MNIST	0.3132	0.5114	0.1305	0.4378	0.1611	0.1628	0.0750	0.9107

the size of 4.0m×4.0m. There are 16 transmitters and 32 receivers located uniformly over the circle at the radius $R = 5.0$m. D is discretized into 64×64 grids to calculate the scattered field by the T-matrix method, while the grids for reconstruction are set to 24×24 to avoid the inverse crime. The scattered field used in training is noiseless for all examples, and 10% white Gaussian noise is added to the scattered fields in testing of synthetic data. According to the above discretization and frequency configurations, the scaling coefficient C is set to 8.0 in synthetic examples. The configurations of the experimental example are similar as above and the difference will be given later in Section III-E.

The Adam optimization method is taken to optimize the attention-assisted pix2pix networks. The generator and discriminator are optimized alternatively during the training process. The updating algorithm of the generator and discriminator is quite similar as that in [35]. The hyperparameters of training process are set as follows. The exponential decay rates are taken as $\beta_1 = 0.9$ and $\beta_2 = 0.999$, respectively. The batch size is set to 1 and totally 40 epochs are done in the training. The initial learning rate is set to 0.0002, and it sequentially decreases to zero from the 21st to the last epoch. The weight parameter α which balances the L_1 loss and L_A loss is set to 100. All network training and testing are done on a workstation (Intel(R) Core(TM) i9-10900X CPU with 128 GB RAM, and GeForce GTX 1080Ti GPU). It takes about 6 hours to train the proposed model with the above training set.

The training losses in different epochs and the validation results are shown in Fig. 5. It is observed that both validation losses reduce smoothly during training and there is no overfitting and underfitting phenomena. After training, we finally chose the testing model as the one with the best SSIM validation loss.

The comparison SOM method is implemented with the T-matrix formulation truncated by the first order multipoles, so as to model the scattering of hybrid scatterers accurately [15]. The results of SOM with zero-order multipole truncation are taken as initials. The dimension of signal subspace in SOM is set to 10 and the total number of iterations is set to 100.

For visualization of reconstruction results, we represent all scatterers as "dielectric" ones, where the PEC scatterers are denoted with $\varepsilon_r = 0$ to mark their shapes and locations. Note that here this practice is only done to distinguish PEC from dielectric scatterers visually.

B. The quality metrics

In this part, we will define quality metrics to evaluate the accuracy of reconstruction algorithms. Considering the magnitude difference of PEC and dielectric scatterers, we define the relative errors of PEC and dielectric scatterers separately, through dividing the reference profile into two parts. The root-mean-square error (RMSE) for PEC scatterer is defined by the $[T]_0$ on PEC scatterer

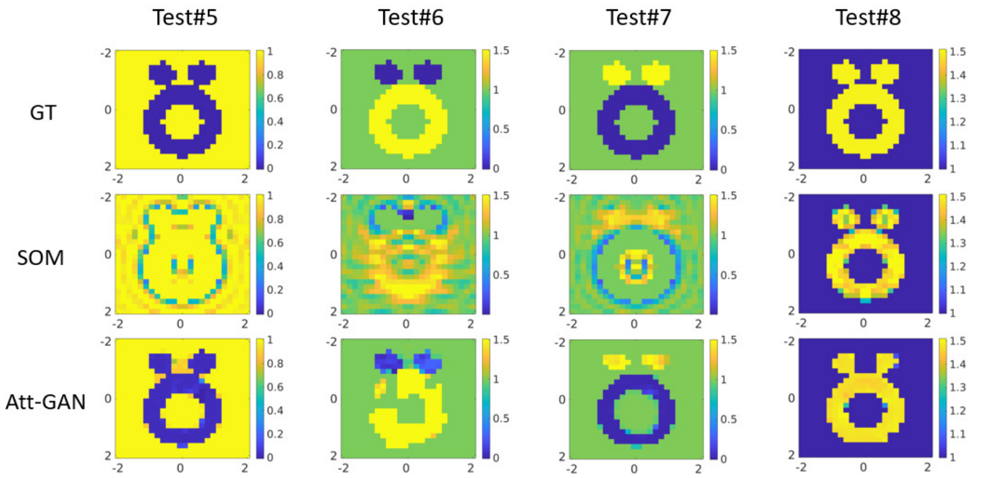

Fig. 7. Reconstruction results of “Austria” profiles with the relative permittivity of ε_r as 1.5. Test#5 to Test#8 are obtained with additional 10% Gaussian noise.

Table II
Comparison of quality metrics for reconstruction results of “Austria” profile with $\varepsilon_r = 1.5$ in Fig. 7

Test	SOM				Att-GAN			
	$E_{\varepsilon_r,diel}$	E_{pec}	E_{diel}	SSIM	$E_{\varepsilon_r,diel}$	E_{pec}	E_{diel}	SSIM
#5	/	0.5430	/	0.2188	/	0.1341	/	0.9566
#6	0.1806	0.4864	0.0568	0.4685	0.2654	0.1823	0.0784	0.7379
#7	0.1453	0.5328	0.0404	0.3353	0.2093	0.2411	0.0521	0.8689
#8	0.0586	/	0.0198	0.8425	0.1004	/	0.0250	0.9399

Table III
Comparison of quality metrics for reconstruction results of “Austria” profile with $\varepsilon_r = 2.0$ in Fig. 8

Test	SOM				Att-GAN			
	$E_{\varepsilon_r,diel}$	E_{pec}	E_{diel}	SSIM	$E_{\varepsilon_r,diel}$	E_{pec}	E_{diel}	SSIM
#9	0.5991	0.4992	0.2109	0.1527	0.2122	0.6329	0.0850	0.7209
#10	0.4259	0.5439	0.1604	0.1651	0.1782	0.1819	0.0766	0.9095
#11	0.5238	/	0.1976	0.1091	0.1453	/	0.0553	0.8750

only,

$$E_{pec} = \sqrt{\frac{1}{N_{pec}} \sum_{(p,q)\in \mathbb{I}_{\mathfrak{P}}} \left(T^{ref}_{i;p,q} - T^{rec}_{i;p,q} \right)^2} \tag{18}$$

where $\mathbb{I}_{\mathfrak{P}}$ indicates the set of indices that belong to PEC scatterers in each reconstructed image, $T^{rec}_{i;p,q}$ and $T^{ref}_{i;p,q}$ are the $[T]_0$ of the ith reconstructed and reference PEC scatterers, respectively, and N_{pec} is the total number of small subunits in $\mathbb{I}_{\mathfrak{P}}$ where only the PEC scatterers distribute.

Similarly, we define the RMSE of $[T]_0$ only on the dielectric scatterers as following,

$$E_{diel} = \sqrt{\frac{1}{N_{diel}} \sum_{(m,n)\in \mathbb{I}_{\mathfrak{D}}} \left(T^{ref}_{j;m,n} - T^{rec}_{j;m,n} \right)^2} \tag{19}$$

where $\mathbb{I}_{\mathfrak{D}}$ indicates the set of indices that belong to dielectric scatterers in each reconstructed image, $T^{rec}_{j;m,n}$ and $T^{ref}_{j;m,n}$ are the jth reconstructed and reference $[T]_0$ of dielectric scatterers, respectively, and N_{diel} is the total number of small subunits in $\mathbb{I}_{\mathfrak{D}}$ occupied by dielectric scatterers.

For dielectric scatterers, we also consider the relative error of ε_r as,

$$E_{\varepsilon_r,diel} = \sqrt{\frac{1}{N_{diel}} \sum_{(m,n)\in \mathbb{I}_{\mathfrak{D}}} \left| \frac{\varepsilon^{ref}_{r;m,n} - \varepsilon^{rec}_{r;m,n}}{\varepsilon^{ref}_{r;m,n}} \right|^2} \tag{20}$$

where $\varepsilon^{rec}_{r;m,n}$ and $\varepsilon^{ref}_{r;m,n}$ are the reconstructed and reference relative permittivity of the dielectric scatterers, respectively.

Finally, in order to evaluate the overall image quality, we also define the structural similarity index (SSIM) between the reference and the reconstructed T-matrix coefficients over the whole DOI. The SSIM is one of the most commonly used perceptual similarity metrics to describe visual structural similarity of two images. More details about the calculation of SSIM can be referred to [36], [37].

C. Test With MNIST Data

In the first example, we test the trained model with another 2500 images randomly selected in the MNIST data set, where 10% white Gaussian noise are added to

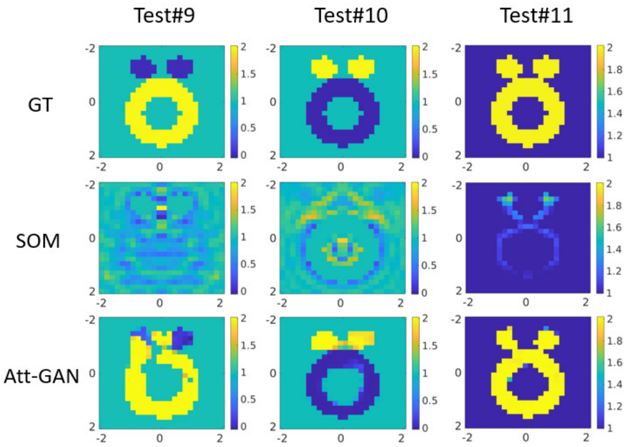

Fig. 8. Reconstruction results of "Austria" profiles with $\varepsilon_r = 2.0$ under 10% white Gaussian noise.

scattered field. We also compare the performance of the proposed method with the SOM method.

The evaluation metrics for all testing samples are summarized in Table I. It is seen that the proposed method achieves quite satisfactory results for the overall 2500 samples with different types of scatterers. Besides, the reconstruction results of four typical cases, Test#1 to Test#4 which include different combinations of scatterers, are demonstrated in Fig. 6. With reference to the ground truth (GT) images, we observe that the SOM method only achieves a good result in Test#4, and the scatterers in the other tests cannot be clearly identified. In comparison, the reconstructions of Att-GAN clearly outperform that of SOM for all the four tests. It proves the capability of the proposed Att-GAN for dealing with ISP with mixed BCs in a unified framework. Particularly, only less than 1 second is taken for reconstructing images using the trained networks. In comparison, the SOM method takes a few seconds to reconstruct a single case. Similar calculation time is also observed for the two methods in subsequent examples.

D. Test With "Austria" Data

In the second example, we verify the generalization capability of the Att-GAN model using the well-known "Austria" profile [38], where the relative permittivity ε_r of the dielectric scatterers is 1.5 and 2, respectively. Meanwhile, 10% white Gaussian noise is added to the scattered field. In this example, we take the same training model as the first example to reconstruct the scatterers.

The reconstruction results for the "Austria" profile with the $\varepsilon_r = 1.5$ are shown in Fig.7. Similar to that of the first example, four different scatterer combinations are studied in Test#5 to Test#8, respectively. In detail, Test#5 is a case of pure PEC scatterers, while Test#8 is a case of pure dielectric scatterers. In contrast, the two disks in Test#6 are PEC and the ring is dielectric. The types of scatterers in Test#7 are completely opposite to that of Test#6. Corresponding to Fig.7, the quality metrics for Test#5 to Test#8 are listed in Table II. We can observe that the proposed Att-GAN well reconstructs different types of scatterers in a unified way. In comparison, the SOM only works well in Test#8 to reconstruct the dielectric scatterers.

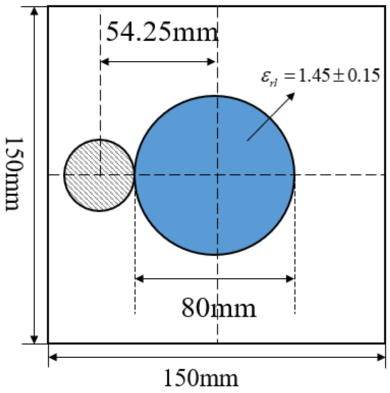

Fig. 9. The "FoamMetExt" profile from Fresnel experimental data.

Besides, we further increase the ε_r of dielectric scatterers in Fig.7 to 2.0 and maintain the other configurations. The reconstruction results are shown in Fig.8, while the corresponding quality metrics are summarized in Table III. In Fig.8, Test#11 is a case of pure dielectric scatterers. The two disks in Test#9 are PEC and the ring is dielectric, while the types of scatterers in Test#10 are completely opposite to that of Test#9. We observe that the results of SOM method are distorted for all cases including the pure dielectric one. Compared to the SOM result in Test#8 with $\varepsilon_r = 1.5$, the result in Test #11 with $\varepsilon_r = 2.0$ converges to a local minimum due to the high nonlinearity. Although the SOM result may be improved by adjusting the initials in this example, we will not discuss it here since it is out of the scope of this paper. In contrast to SOM, the proposed method still gets satisfactory results for all examples. The above reconstruction results of "Austria" profiles show that the Att-GAN consistently outperforms the SOM method. It proves that the trained model of Att-GAN maintains a good generalization capability to challenging examples.

E. Test With Experimental Data

Finally, we verify the proposed method with the experimental data measured by Institue Fresnel [34]. As shown in Fig. 9, the "FoamMetExt" profile consists of a dielectric cylinder and a metallic one, where the blue foam cylinder has a diameter of 80mm with ε_r as 1.45 ± 0.15, and the grey copper tube has a diameter of 28.5mm. There are 18 transmitters evenly distributed around the circle with a radius of 1.67m. For each illumination, there are 241 receivers located at a distance of 1.67m from the origin.

In this example, we take the same configurations as those in Section III-A to prepare the training set, except

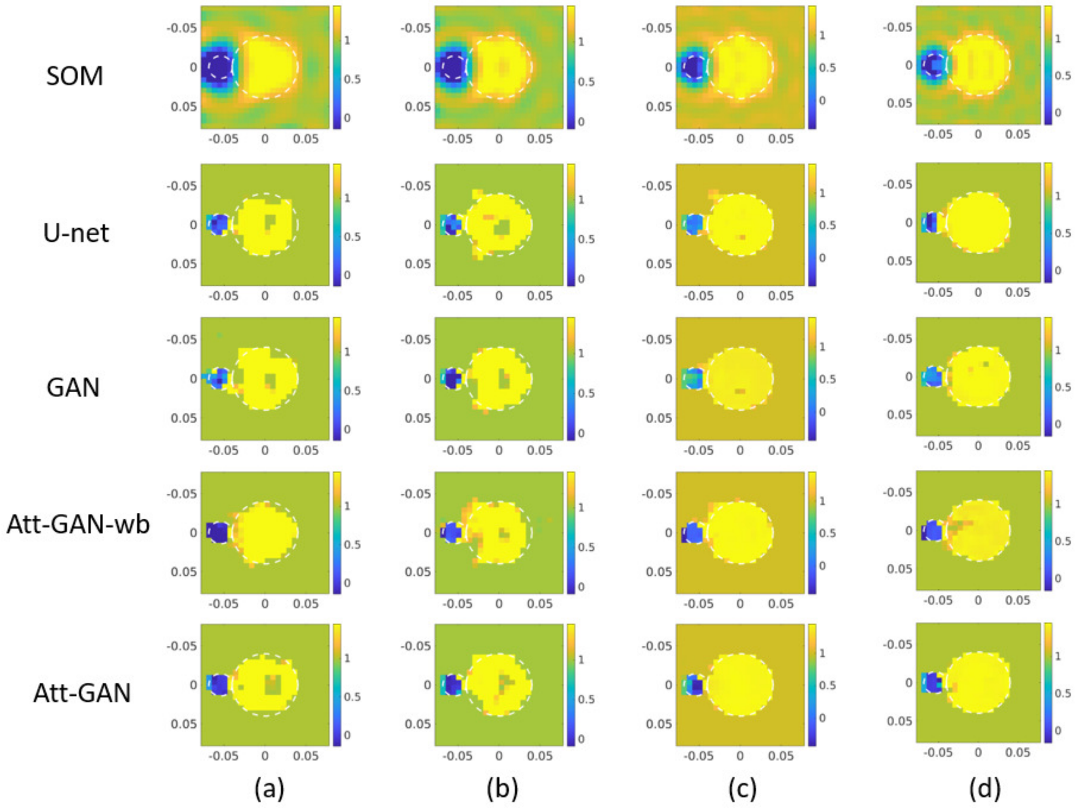

Fig. 10. Reconstruction results of "FoamMetExt" profiles at (a) 3GHz (b) 4GHz (c) 5GHz and (d) 6GHz. It is noted that the dashed lines denote the exact boundaries of cylinders in Fig.9.

Table IV
COMPARISON OF QUALITY METRICS FOR RECONSTRUCTION RESULTS OF "FOAMMETEXT" EXPERIMENTAL DATA IN FIG.10.

Freq.	Method	$E_{\varepsilon_r,diel}$	E_{pec}	E_{diel}	SSIM
3GHz	SOM	0.1732	0.4730	0.0066	0.8395
	U-net	0.1832	0.1939	0.0058	0.9555
	GAN	0.1792	0.2283	0.0058	0.9433
	Att-GAN-wb	0.1760	0.1451	0.0057	0.9584
	Att-GAN	0.1718	0.1005	0.0055	0.9788
4GHz	SOM	0.1479	0.4672	0.0099	0.8430
	U-net	0.1345	0.4117	0.0076	0.8895
	GAN	0.1369	0.3697	0.0077	0.9034
	Att-GAN-wb	0.1390	0.2818	0.0081	0.9082
	Att-GAN	0.1264	0.3320	0.0072	0.9186
5GHz	SOM	0.1176	0.4067	0.0130	0.8485
	U-net	0.0482	0.3365	0.0043	0.9316
	GAN	0.0653	0.3244	0.0061	0.9318
	Att-GAN-wb	0.0432	0.2805	0.0040	0.9219
	Att-GAN	0.0339	0.2965	0.0032	0.9446
6GHz	SOM	0.1055	0.4148	0.0167	0.8364
	U-net	0.0402	0.4007	0.0058	0.9041
	GAN	0.0653	0.3245	0.0086	0.9221
	Att-GAN-wb	0.0879	0.2968	0.0119	0.9168
	Att-GAN	0.0356	0.3349	0.0048	0.9247

that the frequency changes from 300MHz to 3GHz, 4GHz, 5GHz and 6GHz, respectively, and the size of DOI changes from 4.0m × 4.0m to 0.15m × 0.15m. Besides, the scaling coefficient C is also set to 20, 20, 15 and 5, respectively, to be consistent with the frequency change for the training data set. We not only compare the performance of Att-GAN and SOM, but also check the effectiveness of the attention module and the balancing treatment on T-matrix coefficient $[T]_0$. Accordingly, the pix2pix network without attention mechanism is denoted as 'GAN', while the Att-GAN without balancing treatment is represented as "Att-GAN-wb". Finally, the typical U-net method is also compared to demonstrate the benefit of the proposed method. The comparison results of all methods under different frequencies are presented in Fig. 10, and the corresponding quality metrics are listed in Table IV.

It can be seen that the Att-GAN method achieves overall the best performance compared to other methods. In detail, compared to the GAN method, the SSIM is clearly improved, and the quality metrics defined on scatterers have also been improved in general. It indicates that the use of the attention mechanism can enforce the network to learn features concentrating to scatterers, thereby enhancing the reconstruction quality. Meanwhile, compared to Att-GAN-wb, we observe that the imaging quality has been improved after the balancing treatment for all the cases, especially for the dielectric scatterers. But we also observe that the RMSE of PEC scatterers under 4GHz, 5GHz and 6GHz is a little worse after balancing. The reason is that the scaling on $[T]_0$ of PEC will highlight the dielectric scatterers, which brings improvements in reconstruction of dielectric scatterers. In contrast, a certain decline for the reconstruction of PEC may appear. However, the overall

SSIM of all cases is improved, which is also verified visually from the results in Fig. 10. It is noted that the attention mechanism has little influence on the training loss curves. But it can highlight the learning of features by the generator on the unknown scatterers instead of backgrounds, which effectively improves the quality of reconstruction. Finally, the results in Fig. 10 and Table IV also verify that the Att-GAN method achieves better reconstruction results compared to the typical U-net method with only pixel-wise loss.

Although not shown here, the proposed method has also been compared with other typical physics-inspired methods [20], [26] for inversion of pure dielectric scatterers. The Att-GAN achieves similar results compared to those approaches. It shows that the proposed method can also well invert pure dielectric scatterers like those conventional methods. But the advantage of the Att-GAN method is that it can invert ISPs with mixed boundaries.

IV. Conclusion

In this paper, we proposed a unified learning-based method to reconstruct scatterers with mixed BCs. The zero-order T-matrix coefficients of scatterers, instead of the commonly used relative permittivity, have been reconstructed by the attention-assisted pix2pix GAN, without knowing the type of scatterers in advance. The reconstruction of only $[T]_0$ greatly accelerates the imaging speed compared to conventional iterative SOM method. Meanwhile, the introduction of the spatial attention mechanism under the pix2pix GAN framework, as well as the balancing treatment on $[T]_0$ of PEC and dielectric scatterers, guarantees a high-quality reconstruction. Test results on both synthetic and experimental data have validated the superior performance of the proposed method, which effectively expands the application scope of learning-based approaches for solving ISPs with mixed BCs.

References

[1] X. Chen, *Computational methods for electromagnetic inverse scattering*. Wiley Online Library, 2018.

[2] L.-P. Song, C. Yu, and Q. H. Liu, "Through-wall imaging (TWI) by radar: 2-D tomographic results and analyses," *IEEE Transactions on Geoscience and Remote Sensing*, vol. 43, no. 12, pp. 2793–2798, 2005.

[3] T. Deisboeck and J. Y. Kresh, *Complex systems science in biomedicine*. Springer Science & Business Media, 2007.

[4] R. Persico, *Introduction to ground penetrating radar: inverse scattering and data processing*. John Wiley & Sons, 2014.

[5] Y. Zhong and X. Chen, "Twofold subspace-based optimization method for solving inverse scattering problems," *Inverse Problems*, vol. 25, no. 8, p. 085003, 2009.

[6] Y. Zhong, X. Chen, and K. Agarwal, "An improved subspace-based optimization method and its implementation in solving three-dimensional inverse problems," *IEEE Transactions on Geoscience and Remote Sensing*, vol. 48, no. 10, pp. 3763–3768, 2010.

[7] X. Chen, "Subspace-based optimization method for solving inverse-scattering problems," *IEEE Transactions on Geoscience and Remote Sensing*, vol. 48, no. 1, pp. 42–49, 2009.

[8] A. Qing, C. K. Lee, and L. Jen, "Electromagnetic inverse scattering of two-dimensional perfectly conducting objects by real-coded genetic algorithm," *IEEE Transactions on Geoscience and Remote Sensing*, vol. 39, no. 3, pp. 665–676, 2001.

[9] A. Qing, "Electromagnetic inverse scattering of multiple two-dimensional perfectly conducting objects by the differential evolution strategy," *IEEE Transactions on Antennas and Propagation*, vol. 51, no. 6, pp. 1251–1262, 2003.

[10] X. Ye, X. Chen, Y. Zhong, and K. Agarwal, "Subspace-based optimization method for reconstructing perfectly electric conductors," *Progress in Electromagnetics Research*, vol. 100, pp. 119–128, 2010.

[11] P. Waterman, "Matrix formulation of electromagnetic scattering," *Proceedings of the IEEE*, vol. 53, no. 8, pp. 805–812, 1965.

[12] W. Chew and Y. Wang, "A fast algorithm for solution of a scattering problem using a recursive aggregate τ matrix method," *Microwave and Optical Technology Letters*, vol. 3, no. 5, pp. 164–169, 1990.

[13] G. P. Otto and W. C. Chew, "Microwave inverse scattering/spl minus/local shape function imaging for improved resolution of strong scatterers," *IEEE Transactions on Microwave Theory and Techniques*, vol. 42, no. 1, pp. 137–141, 1994.

[14] J. Lin and W. C. Chew, "BiCG-FFT T-matrix method for solving for the scattering solution from inhomogeneous bodies," *IEEE Transactions on Microwave Theory and Techniques*, vol. 44, no. 7, pp. 1150–1155, 1996.

[15] X. Ye, X. Chen, Y. Zhong, and R. Song, "Simultaneous reconstruction of dielectric and perfectly conducting scatterers via T−matrix method," *IEEE Transactions on Antennas and Propagation*, vol. 61, no. 7, pp. 3774–3781, 2013.

[16] R. Song, X. Ye, and X. Chen, "Reconstruction of scatterers with four different boundary conditions by T-matrix method," *Inverse Problems in Science and Engineering*, vol. 23, no. 4, pp. 601–616, 2015.

[17] A. Massa, D. Marcantonio, X. Chen, M. Li, and M. Salucci, "DNNs as applied to electromagnetics, antennas, and propagation-A review," *IEEE Antennas and Wireless Propagation Letters*, vol. 18, no. 11, pp. 2225–2229, 2019.

[18] X. Chen, Z. Wei, M. Li, and P. Rocca, "A review of deep learning approaches for inverse scattering problems (invited review)," *Progress In Electromagnetics Research*, vol. 167, pp. 67–81, 2020.

[19] J. E. Fajardo, J. Galván, F. Vericat, C. M. Carlevaro, and R. M. Irastorza, "Phaseless microwave imaging of dielectric cylinders: An artificial neural networks-based approach," *Progress In Electromagnetics Research*, vol. 166, pp. 95–105, 2019.

[20] Z. Wei and X. Chen, "Deep-learning schemes for full-wave nonlinear inverse scattering problems," *IEEE Transactions on Geoscience and Remote Sensing*, vol. 57, no. 4, pp. 1849–1860, 2018.

[21] H. M. Yao, E. Wei, and L. Jiang, "Two-step enhanced deep learning approach for electromagnetic inverse scattering problems," *IEEE Antennas and Wireless Propagation Letters*, vol. 18, no. 11, pp. 2254–2258, 2019.

[22] R. Guo, X. Song, M. Li, F. Yang, S. Xu, and A. Abubakar, "Supervised descent learning technique for 2-D microwave imaging," *IEEE Transactions on Antennas and Propagation*, vol. 67, no. 5, pp. 3550–3554, 2019.

[23] J. Adler and O. Öktem, "Solving ill-posed inverse problems using iterative deep neural networks," *Inverse Problems*, vol. 33, no. 12, p. 124007, 2017.

[24] G. Chen, P. Shah, J. Stang, and M. Moghaddam, "Learning-assisted multimodality dielectric imaging," *IEEE Transactions on Antennas and Propagation*, vol. 68, no. 3, pp. 2356–2369, 2019.

[25] L. Li, L. G. Wang, F. L. Teixeira, C. Liu, A. Nehorai, and T. J. Cui, "DeepNIS: Deep neural network for nonlinear electromagnetic inverse scattering," *IEEE Transactions on Antennas and Propagation*, vol. 67, no. 3, pp. 1819–1825, 2018.

[26] Z. Wei and X. Chen, "Physics-inspired convolutional neural network for solving full-wave inverse scattering problems," *IEEE Transactions on Antennas and Propagation*, vol. 67, no. 9, pp. 6138–6148, 2019.

[27] J. Xiao, J. Li, Y. Chen, F. Han, and Q. H. Liu, "Fast electromagnetic inversion of inhomogeneous scatterers embedded in layered media by born approximation and 3-D U-Net," *IEEE Geoscience and Remote Sensing Letters*, vol. 17, no. 10, pp. 1677–1681, 2019.

[28] R. Guo, Z. Lin, T. Shan, X. Song, M. Li, F. Yang, S. Xu, and A. Abubakar, "Physics embedded deep neural network for solving full-wave inverse scattering problems," *IEEE Transactions on Antennas and Propagation*, early access,2021.

[29] P. Isola, J.-Y. Zhu, T. Zhou, and A. A. Efros, "Image-to-image translation with conditional adversarial networks," in *Proceedings*

of the IEEE conference on computer vision and pattern recognition, 2017, pp. 1125–1134.

[30] O. Oktay, J. Schlemper, L. L. Folgoc, M. Lee, M. Heinrich, K. Misawa, K. Mori, S. McDonagh, N. Y. Hammerla, B. Kainz *et al.*, "Attention u-net: Learning where to look for the pancreas," in *2018 1st Conference on Medical Imaging with Deep Learning (MIDL 2018), Amsterdam, The Netherlands*, 2018.

[31] A. Z. Elsherbeni, A. Kishk *et al.*, "Modeling of cylindrical objects by circular dielectric and conducting cylinders," *IEEE Transactions on Antennas and Propagation*, vol. 40, no. 1, pp. 96–99, 1992.

[32] K. Belkebir, P. C. Chaumet, and A. Sentenac, "Superresolution in total internal reflection tomography," *Journal of the Optical Society of America A*, vol. 22, no. 9, pp. 1889–1897, 2005.

[33] Y. LeCun, L. Bottou, Y. Bengio, and P. Haffner, "Gradient-based learning applied to document recognition," *Proceedings of the IEEE*, vol. 86, no. 11, pp. 2278–2324, 1998.

[34] J.-M. Geffrin, P. Sabouroux, and C. Eyraud, "Free space experimental scattering database continuation: experimental set-up and measurement precision," *Inverse Problems*, vol. 21, no. 6, p. S117, 2005.

[35] R. Song, Y. Huang, K. Xu, X. Ye, C. Li, and X. Chen, "Electromagnetic inverse scattering with perceptual generative adversarial networks," *IEEE Transactions on Computational Imaging*, vol. 7, pp. 689–699, 2021.

[36] J. Snell, K. Ridgeway, R. Liao, B. D. Roads, M. C. Mozer, and R. S. Zemel, "Learning to generate images with perceptual similarity metrics," in *2017 IEEE International Conference on Image Processing (ICIP)*. IEEE, 2017, pp. 4277–4281.

[37] Y. Huang, R. Song, K. Xu, X. Ye, C. Li, and X. Chen, "Deep learning-based inverse scattering with structural similarity loss functions," *IEEE Sensors Journal*, vol. 21, no. 4, pp. 4900–4907, 2020.

[38] K. Belkebir and A. Tijhuis, "Using multiple frequency information in the iterative solution of a two-dimensional nonlinear inverse problem," in *Proceedings Progress in Electromagnetics Research Symposium, PIERS 1996, 8 July 1996, Innsbruck, Germany*. Universität Innsbruck, 1996.

Rencheng Song received the B.S. degree from Jilin University, Changchun, China, in 2005, and the Ph.D. degree from Zhejiang University, Hangzhou, China in 2010, both in computational mathematics. From 2010 to 2012, he was a Research Fellow with the Department of Electrical and Computer Engineering at National University of Singapore, Singapore. From 2013 to 2017, he was a Principal Scientist with Halliburton Far East Pte Ltd, Singapore. Since May 2017, he has been with the Department of Biomedical Engineering at Hefei University of Technology, Hefei, China, as an associate professor. His research interests include electromagnetic/video-based intelligent perceptions, such as electromagnetic imaging, remote photoplethysmography, and physics-inspired machine learning methods.

Youyou Huang received the B.E. degree in Automation from Hefei University of Technology, Hefei, China, in 2019. She is currently pursuing the M.S. degree in Hefei University of Technology.Her current research interests include microwave imaging and electromagnetic inverse scattering problems.

Xiuzhu Ye (S'11-M'12-SM'19) received the B.E. degree in Telecommunication Engineering from Harbin Institute of Technology, Harbin, China, in 2008 and the Ph.D. degree from Department of Electrical and Computer Engineering in National University of Singapore, Singapore, in 2012.From 2012 to 2013, she worked in Department of Electrical and Computer Engineering, National University of Singapore as a Research Fellow. Since 2013, she worked as Assistant Professor in Beihang University. Since 2019, she has been an Associate Professor with School of Information and Electronics, Beijing Institute of Technology. Her research areas are electromagnetic inverse problems, microwave imaging methods, antenna designing and machine learning. Dr. Ye has served on review boards of various technical journals, including IEEE Transactions on Antenna and Propagation, IEEE Transactions on Microwave Theory and Techniques, Radio Science and Optics Express.

Kuiwen Xu received the B.E. degree from Hangzhou Dianzi University, and the Ph.D. degree from Zhejiang University, Hangzhou, China, in 2009 and 2014, respectively.From 2012 to 2013, he was a Visiting Ph.D. Student with the National University of Singapore, Singapore. From 2014 to 2015, he was a Senior Researcher with Huawei Technologies Company, Ltd., Hangzhou. He was invited to the State Key Laboratory of Terahertz and Millimeter Waves, City University of Hong Kong, Hong Kong, as a Visiting Professor, in 2018. Since September 2015, he has been with Hangzhou Dianzi University, Hangzhou, where he is currently a Professor. He has published more than 50 journal articles on electromagnetics inverse problems, antenna design and synthesis, microwave measurement and sensing. His research interests include but not limited to computational imaging and electromagnetics inverse problems, machine learning-based wireless sensing and imaging, and new concept antennas (MIMO antenna, Meta-based array-antenna, etc.).

Chang Li received the B.S. degree in information and computing science from the Wuhan Institute of Technology, Wuhan, China, in 2012, and the Ph.D. degree in circuits and systems from the School of Electronic Information and Communications, Huazhong University of Science and Technology, Wuhan, in 2018.

He is currently a Lecturer with the Department of Biomedical Engineering, Hefei University of Technology, Hefei, China. His research interests include biomedical signal processing, hyperspectral image analysis, computer vision, pattern recognition, and machine learning.

Xun Chen (Senior Member, IEEE) received the B.Sc. degree in electrical engineering from the University of Science and Technology of China in 2009 and the Ph.D. degree in biomedical engineering from The University of British Columbia (UBC), Canada. He has been a Research Scientist with the Department of Electrical and Computer Engineering, UBC. He is currently a Full Professor and the Head of the Department of Electrical Engineering and Information Science, University of Science and Technology of China. He has published over 100 scientific articles in prestigious IEEE/Elsevier journals and conferences. His research interests include statistical signal processing and machine learning in biomedical applications. He is serving as an Area Editor for Signal Processing: Image Communication and an Associate Editor for IEEE Signal Processing Letters and Frontiers in Neuroscience.